

Superconductivity and suppressed monoclinic distortion in FeTe films enabled by higher-order epitaxy

Received: 28 April 2025

Accepted: 24 October 2025

Published online: 05 December 2025

 Check for updates

Yuki Sato ¹✉, Soma Nagahama ², Shunsuke Kitou ³, Hajime Sagayama ⁴, Ilya Belopolski ¹, Ryutaro Yoshimi ^{1,3}, Minoru Kawamura ¹, Atsushi Tsukazaki ^{2,5}, Naoya Kanazawa ⁶, Takuya Nomoto ⁷, Ryotaro Arita ^{1,8}, Taka-hisa Arima ^{1,3}, Masashi Kawasaki ^{1,2} & Yoshinori Tokura ^{1,2,9}✉

Molecular beam epitaxy enables the growth of thin film materials with novel properties and functionalities. Typically, the lattice constants of films and substrates are designed to match to minimise disorders and strains. However, significant lattice mismatches can result in higher-order epitaxy, where commensurate growth occurs with a period defined by integer multiples of the lattice constants. Despite its potential, higher-order epitaxy is rarely used to enhance material properties or induce emergent phenomena. Here, we report single-crystalline FeTe films grown via 6:5 commensurate higher-order epitaxy on CdTe(001) substrates. Scanning transmission electron microscopy reveals self-organised periodic interstitials near the interface, arising from higher-order lattice matching. Synchrotron x-ray diffraction shows that the tetragonal-to-monoclinic structural transition in bulk FeTe is strongly suppressed. Remarkably, these films exhibit substrate-selective two-dimensional superconductivity, likely due to suppressed monoclinic distortion. These findings demonstrate the potential of higher-order epitaxy as a tool to control materials and inducing emergent phenomena.

Engineering materials in thin film form not only enhances our understanding of quantum phenomena but also provides knobs to tune material properties. Among various deposition techniques, molecular beam epitaxy (MBE)—a method where films are grown layer by layer with lattice matching to a substrate—is one of the most powerful tools for fabricating a wide variety of thin films and heterostructures. It offers exceptional control over structure and composition, enabling novel properties and functionalities that go beyond those of bulk crystals^{1–7}. In materials engineering, achieving high-quality materials with minimal disorders, such as defects, misorientation and

dislocations, is crucial because quantum transport phenomena often favour clean systems with long scattering times³. In contrast, it is widely known that significant lattice mismatches between a film and a substrate can sometimes result in higher-order epitaxy, also referred to as domain-matching epitaxy, where commensurate growth occurs with a long period defined by integer multiples of the lattice constants^{8–11}. Although such growth modes are typically avoided as they introduce unnecessary disorder into crystals, it has recently been suggested that spatially modulated strain, caused by mismatches, can be used to control the topological properties of materials¹². Despite its

¹RIKEN Center for Emergent Matter Science (CEMS), Wako, Japan. ²Department of Applied Physics and Quantum-phase Electronics Center (QPEC), University of Tokyo, Tokyo, Japan. ³Department of Advanced Materials Science, University of Tokyo, Kashiwa, Japan. ⁴Institute of Materials Structure Science, High Energy Accelerator Research Organization, Tsukuba, Japan. ⁵Institute for Materials Research (IMR), Tohoku University, Sendai, Japan. ⁶Institute of Industrial Science, University of Tokyo, Tokyo, Japan. ⁷Department of Physics, Tokyo Metropolitan University, Hachioji, Tokyo, Japan. ⁸Department of Physics, University of Tokyo, Tokyo, Japan. ⁹Tokyo College, University of Tokyo, Tokyo, Japan. ✉e-mail: yuki.sato.yj@riken.jp; tokura@riken.jp

potential, there are few examples of higher-order epitaxy being utilised to enhance materials properties or induce novel quantum phenomena¹³.

Iron chalcogenides are one of the most attractive materials platforms for studying the interplay between thin films and substrates, as exemplified by the significant enhancement of the superconducting transition temperature T_c in monolayer FeSe grown on SrTiO₃ (STO), from a bulk value of 10 K to above 50 K in the monolayer form⁴. The Fe(Se,Te) (FST) system has attracted significant interest as a candidate topological superconductor driven by strong spin-orbit coupling from Te, where a Majorana zero mode is expected to emerge at the core of vortex^{14–16}. It is also utilised for a building block for an artificial topological superconductor, where FST is proximitised with topological insulators^{17,18}. FeTe is the other end compound of the FST series and is a non-superconducting antiferromagnetic (AFM) metal. It has a tetragonal $P4/nmm$ crystalline structure consisting of van der Waals-stacked iron-chalcogenide square lattices at room temperature (Fig. 1a). FeTe crystals with minimal excess iron amount undergo a transition to the monoclinic $P2_1/m$ phase at the structural transition temperature $T_s \sim 70$ K, below which in-plane anisotropy develops ($a/b > 1$) and the c -axis tilts slightly towards the a -axis ($\beta < 90^\circ$) (Fig. 1b)¹⁹. This monoclinic lattice distortion is accompanied by the emergence of a double-stripe AFM order with a magnetic vector $Q = (\pi, 0)$ in the reciprocal space of the tetragonal lattice with two iron atoms per unit cell (UC)²⁰. Neutron scattering experiments reveal that superconductivity emerges when the $(\pi, 0)$ magnetic correlations are

suppressed by partly substituting Se for Te, suggesting that the AFM order is detrimental to superconductivity²¹.

Results and Discussion

In this paper, we report growth of single-crystalline higher-order epitaxial superconducting FeTe films using the MBE technique grown on cubic zinc-blende CdTe(001) substrates (Fig. 1c), (See Methods and¹⁷ for more details about sample fabrication). For comparison, we also grew FeTe films on cubic perovskite STO(001) substrates (Fig. 1d). FeTe/CdTe films appear to be single-crystalline with the crystalline orientation of FeTe highly aligned to that of CdTe. Figure 1e shows an XRD θ - 2θ profile for a typical FeTe/CdTe film. We observe sharp peaks attributed to FeTe (0 0 n) or CdTe (0 0 $2m$), where n and m are integers, indicating that the FeTe (0 0 1) plane is aligned parallel to the substrate normal, i.e., FeTe [001] \parallel CdTe [001]. The high crystalline quality of the film is further supported by a rocking curve for the FeTe (0 0 1) reflection. As shown in Fig. 1f, the rocking curve for FeTe/CdTe exhibits a sharp signal with a small full-width at half maximum (FWHM) of 0.6° , whereas that for FeTe/STO shows a much broader value of 1.8° . Furthermore, the XRD azimuthal angle φ -scan for the asymmetric FeTe (1 0 4) reflection shows a clear 4-fold oscillation, following the same trend as CdTe (1 1 5) (Fig. 1g). The result is consistent with the tetragonal crystal structure and indicates a high lateral orientation of the FeTe film, where FeTe [100] \parallel CdTe [110]. This lateral orientation is further confirmed by atomic force microscopy measurements, which reveal well-defined square-patterned steps and terraces with edges

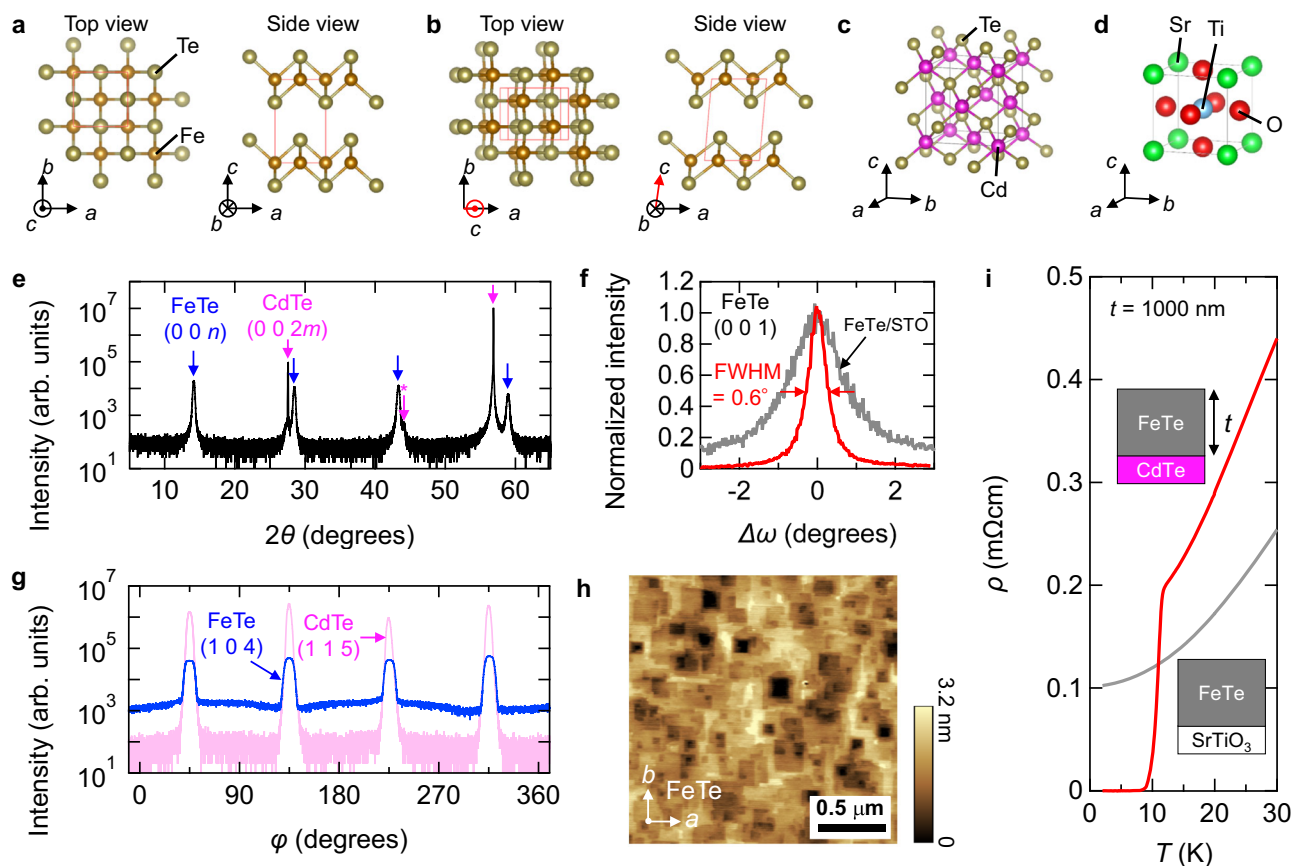


Fig. 1 | Crystal structures, characterisation, and substrate-selective superconductivity of FeTe films. **a** High-temperature tetragonal and **b** low-temperature monoclinic crystal structures of FeTe²². The red boxes indicate the unit cell. The in-plane anisotropy a/b and the tilt angle $\pi/2 - \beta$ are slightly exaggerated to emphasize the monoclinic distortion. **c** Crystal structure of CdTe. **d** Crystal structure of SrTiO₃ (STO). **e** X-ray diffraction (XRD) θ - 2θ profile for an FeTe/CdTe film. The blue and magenta arrows indicate FeTe (0 0 n) and CdTe (0 0 $2m$) reflections, respectively,

where n and m are integers. The asterisk demotes an impurity phase of NaCl-type CdTe. **f** XRD rocking curves for the FeTe (0 0 1) reflection for FeTe/CdTe (red) and FeTe/STO (grey) films. **g** XRD azimuthal profiles for the asymmetric Bragg reflections for FeTe (1 0 4) (blue) and CdTe (1 1 5) (magenta). **h** Atomic force microscopy image for an FeTe/CdTe film after vacuum annealing. The scale bar represents $0.5 \mu\text{m}$. **i** Temperature dependence of resistivity for 1000-nm-thick FeTe films grown on CdTe (red) and STO (grey).

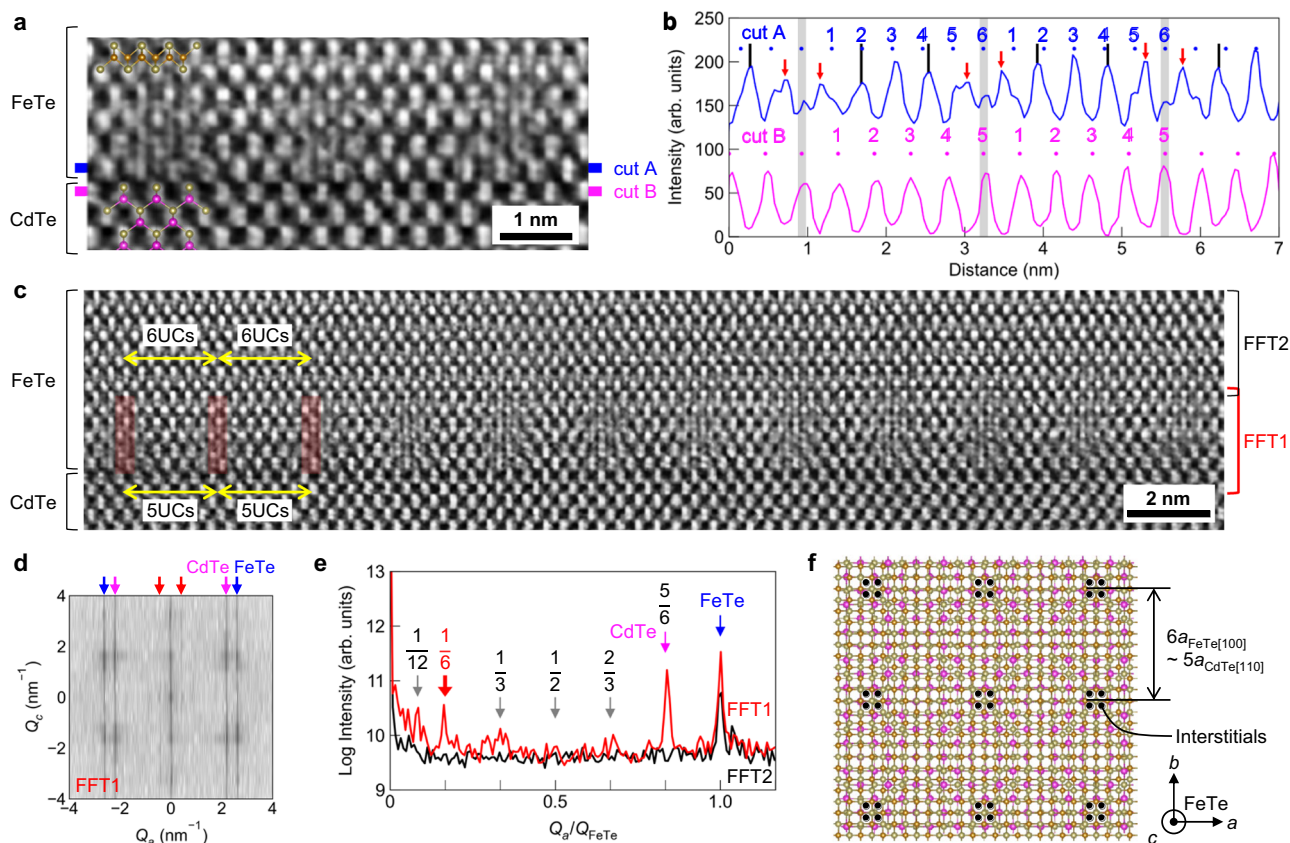


Fig. 2 | Real-space observation of self-organised periodic interstitial modulation near FeTe/CdTe interface. **a** Cross-sectional HAADF-STEM image near an FeTe/CdTe interface. The yellow, brown, and magenta spheres indicate Te, Fe, and Cd atoms, respectively. **b** Integrated-intensity profiles along the cut A and B indicated in **a**. The dots above the profile indicate the equilibrium position for each atom. The grey areas indicate the nearest sites where the interfacial ions approach most closely. The red arrows represent the interfacial interstitials. The vertical solid black lines represent peak position for the sites 2 and 4, showing a slight modulation from the equilibrium towards the nearest sites. **c** Wide-area HAADF-STEM image near an FeTe/CdTe interface. The red shaded region indicates the position of the periodic interstitials. The yellow arrows denote the period of modulation, which

corresponds to 6 unit cells (UCs) of FeTe, which approximately equals to 5 UCs of CdTe. Areas labelled as FFT1 and FFT2 correspond to the regions where fast Fourier transformation (FFT) was performed. **d** FFT image taken within FFT1 in **c**. The blue, magenta, and red arrows indicate Bragg peaks for FeTe, CdTe, and the interfacial modulation, respectively. **e** FFT profiles integrated along Q_c as a function of Q_a divided by the wave number Q_{FeTe} , corresponding to a Bragg peak of FeTe (0 1 0). The red and black lines correspond to the results taken in FFT1 and FFT2, respectively. The blue, magenta, and red arrows are the same as **d**, while the grey arrows indicate harmonics of the interfacial modulation, which appear at fractions of Q_{FeTe} . **f** Top-view schematics of the 6×6 superlattice of the interfacial interstitials.

aligned to CdTe $\langle 110 \rangle$ (Fig. 1h). Remarkably, FeTe/CdTe films exhibit superconductivity with an onset critical temperature $T_c \sim 12$ K, whereas FeTe/STO films grown under the exactly same conditions do not show any superconducting onset down to 2 K (Fig. 1i). We note that the zero resistivity in FeTe/CdTe was not achieved in our previous works, where a partial superconducting transition is observed and zero resistivity appears only when FeTe is interfaced with Bi_2Te_3 ^{17,22}. The zero-resistivity in the current work is achieved by further optimizing growth conditions, such as growth rate and Te-annealing temperature and time. While it has been reported that superconductivity in FeTe can be induced by oxygen incorporation, this typically requires aggressive methods such as exposure to atmosphere for weeks or annealing under oxygen flow^{23,24}. To rule out this possibility, we simultaneously synthesised, in-situ Te-capped, and measured those two films within a day. The results suggest that the substrate-selective superconductivity is an intrinsic property of FeTe/CdTe. These observations motivate a detailed investigation into the crystal structure of FeTe/CdTe.

It is worth noting that the in-plane lattice mismatch between FeTe ($a_{FeTe[100]} = 0.383$ nm) and CdTe ($a_{CdTe[110]} = 0.458$ nm) is as large as $\sim 20\%$, whereas that between FeTe and STO ($a_{STO[100]} = 0.390$ nm) is relatively small at $\sim 1.8\%$. Given this, it is somewhat surprising that

FeTe/CdTe films exhibit apparently higher crystalline quality than FeTe/STO films (See Fig. S1 for further characterisation of FeTe/STO). This counterintuitive result can be attributed to higher-order epitaxy, characterised by a 6:5 commensuration between FeTe and CdTe, as we show in the following. Figure 2a displays a cross-sectional high-angle annular dark-field scanning transmission electron microscopy (HAADF-STEM) image of the FeTe/CdTe interface viewed from FeTe $[100] \parallel$ CdTe $[110]$ at room temperature. The interface between FeTe and CdTe is clearly resolved with atomic resolution, as indicated by the overlaid cartoons. Figure 2b presents line profiles along cut A (the bottommost layer of FeTe) and B (the topmost layer of CdTe). While the two profiles differ in modulation period due to the substantial lattice mismatch, there are distinct nearest sites where two atoms closely approach each other. These sites recur every $6a_{FeTe[100]}$ or $5a_{CdTe[110]}$, as highlighted by the grey-shaded regions in Fig. 2b. This higher-order lattice matching results in a considerably small residual mismatch, calculated as $(6a_{FeTe[100]} - 5a_{CdTe[110]})/6a_{FeTe[100]} \sim +0.35\%$. These results confirm the successful realisation of higher-order epitaxy in FeTe/CdTe films.

The higher-order epitaxy appears to be stabilised by the introduction of self-organised interstitials and periodic displacement only near the interface. As highlighted by the red arrows in Fig. 2b, a pair of

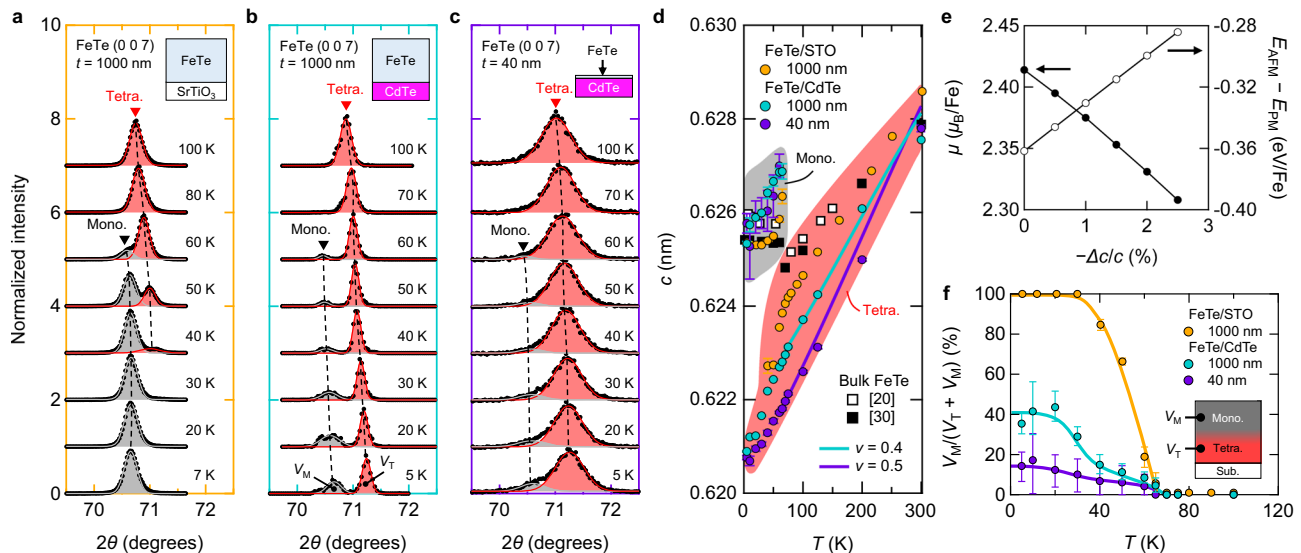


Fig. 3 | Suppression of monoclinic lattice distortion in FeTe/CdTe films. a–c XRD θ - 2θ profiles around the FeTe (0 0 7) Bragg reflection for **a** FeTe1000/STO, **b** FeTe1000/CdTe, and **c** FeTe40/CdTe. Each profile is vertically shifted for clarity. Red and grey curves are Gaussian fittings for the tetragonal and monoclinic phases, respectively. Vertical dashed lines are guides for eyes. **d** Temperature dependence of the lattice parameter c deduced from the FeTe (0 0 7) reflections. Orange, cyan, and purple markers denote FeTe1000/STO, FeTe1000/CdTe, and FeTe40/CdTe, respectively. White and black squares are c for bulk single crystals reported by neutron²⁰ and XRD³⁰ studies. Cyan and purple lines are simulations for the Poisson

ratios $\nu = 0.4$ and 0.5 , respectively, assuming perfect clamping to the CdTe substrate. The data highlighted in red and grey areas are those for tetragonal and monoclinic phases, respectively. The error bars represent the standard deviation derived from fittings. **e** Fe moments μ and energy difference between AFM and paramagnetic phases, $E_{\text{AFM}} - E_{\text{PM}}$, as a function of out-of-plane compressive strain $-\Delta c/c$, obtained by first-principles calculation. **f** Temperature dependence of the volume fraction of the monoclinic phase, $V_M/(V_T + V_M)$. The inset schematically depicts a film with a phase separation into monoclinic and tetragonal. The lines are guides for eyes. The error bars represent the standard deviation derived from fittings.

additional peaks is observed adjacent to the nearest sites. These interstitials, likely intercalated to reduce interfacial energy associated with the higher-order epitaxy, do not belong to the crystal structures of either FeTe or CdTe, breaking the translational symmetry of FeTe. Such periodic interfacial interstitials have not been observed in other van der Waals-epitaxial systems such as FeSe/STO and FeSe/MgO^{25–27}. Typically, higher-order epitaxial films relax the strain through periodic or random dislocations, characterised by Burgers vectors oriented in the in-plane direction^{10,28,29}. However, in the present system, no apparent dislocation is observed at the interface, and both FeTe and CdTe retain their original crystal structure except for the interstitials. Moreover, we found a slight displacement of atoms at certain sites, marked as 2 and 4 in Fig. 2b, from the equilibrium position. This displacement can be viewed as a local strain that is not uniform, but spatially modulates.

We examine a HAADF-STEM image of an FeTe/CdTe interface over a wider observation frame (Fig. 2c). Interestingly, the interstitials at the FeTe/CdTe interface extend slightly along FeTe [001] into a few UCs, forming discernible *nodes* that periodically recur along FeTe [010], spanning the entire observation window. Figure 2d displays the fast Fourier transform (FFT) image derived from the HAADF-STEM image near the interface, labelled as FFT1 in Fig. 2c. In addition to the Bragg peaks corresponding to FeTe and CdTe, we observe additional peaks associated with the modulation from higher-order epitaxy. To highlight this, Fig. 2e shows a profile integrated along the Q_c direction as a function of Q_a . Here the horizontal axis is normalised by the reciprocal lattice vector of FeTe, Q_{FeTe} . Apart from the primary Bragg peaks, a distinct peak appears at $Q_a/Q_{\text{FeTe}} = 1/6$, consistent with the modulation period of $6a_{\text{FeTe}[100]}$. This peak indicates that the interstitials extend coherently over the interface and create intrinsic structural modulation rather than extrinsic effects, such as moiré interference patterns along the electron beam direction. In addition to the primary modulation mode at $Q_a/Q_{\text{FeTe}} = 1/6$, related modes at $Q_a/Q_{\text{FeTe}} = 1/3, 1/2$, and $2/3$ are faintly resolved. A mode at $Q_a/Q_{\text{FeTe}} = 1/12$

appears with an intensity somewhat comparable to the $1/6$ mode, hinting at the possible involvement of an additional modulation with a period of $12a_{\text{FeTe}[100]}$ in stabilising the interface. When the FFT is performed on the image taken 3 UCs away from the interface (FFT2), the peak at $Q_a/Q_{\text{FeTe}} = 1/6$ is not discernible. This suggests that the higher-order epitaxy occurs only near the interface, transitioning to the conventional van der Waals epitaxy at a greater distance. Figure 2f schematically illustrates the FeTe/CdTe interface from the top (FeTe [001]), where the interstitial pairs form superlattice along the interface, resulting in a characteristic 6×6 modulation. This modulation is also confirmed by Reflection High Energy Electron Diffraction (RHEED), which reveals additional pronounced peaks corresponding to the superlattice only when a few UCs of FeTe are deposited (Fig. S3). Identifying the chemical nature of the interstitials, however, remains challenging, as their close spacing with other elements exceeds the resolution limits of our current experiments.

As higher-order epitaxy is a characteristic of FeTe/CdTe films, it is tempting to attribute the substrate-selective superconductivity to some consequences resulting from this epitaxy. To access a potential link between the superconductivity and crystal structure at low temperatures, we performed temperature (T)-dependent synchrotron XRD experiments on FeTe films. First, as a reference, we measured a thick FeTe/STO film with a thickness t of 1000 nm, denoted as FeTe1000/STO (Fig. 3a). At $T = 100$ K, (0 0 7) Bragg reflection appears as a single peak in the θ - 2θ profile. As T decreases, the intensity of this peak steadily diminishes, while another peak begins to emerge at lower angles ($2\theta \sim 70.7^\circ$) below $T_s \sim 60$ K. At a base temperature of 7 K, the higher-angle peak disappears completely, leaving a single peak at the lower angle. This discrete shift in the 2θ peak position is a consequence of the tetragonal-to-monoclinic structural transition, as reported in bulk crystals^{20,30} (See Fig. S4 for reciprocal space mappings).

Next, we performed θ - 2θ XRD scans for thick and thin FeTe/CdTe films with $t = 1000$ nm (FeTe1000/CdTe) and 40 nm (FeTe40/CdTe), as shown in Fig. 3b, c. Hereafter, FeTe t /CdTe denotes a t -nm-thick FeTe

film grown on CdTe(100) substrate. In the thick FeTe1000/CdTe film, similar to the FeTe1000/STO film, the lower-angle peak associated with the monoclinic phase develops below T_s . Interestingly, in FeTe1000/CdTe, the higher-angle peak associated with the tetragonal phase remains prominent even below T_s , and the θ - 2θ scan reveals a distinct double-peak structure at low temperatures. This double-peak structure indicates the coexistence of tetragonal and monoclinic phases in FeTe1000/CdTe. Notably, the tetragonal phase exhibits a stronger intensity compared to the monoclinic phase, suggesting that, contrary to bulk crystals, the tetragonal phase dominates in FeTe1000/CdTe at low temperatures. The contrasting behaviour observed in FeTe1000/CdTe underscores the critical role of substrate-induced effect, such as cramping, in suppressing monoclinic distortion. Furthermore, in the thin FeTe40/CdTe film, the tetragonal phase is even more dominant, as evidenced by the θ - 2θ scans, which shows a single major peak with a slight asymmetry developing below T_s . This asymmetry is attributed to a small portion exhibiting monoclinic distortion. The double Gaussian fitting at each temperature successfully separates the two components in the data.

In Fig. 3d, we summarise the out-of-plane lattice constant c , estimated using single or double Gaussian fittings, as a function of T , alongside values for bulk crystals reported in the literature^{20,30}. At 300 K, the c -values of the films are close to those of the bulk crystals, suggesting that strain from the substrates is minimal. Upon cooling, c of the films decreases, with the largest slope of dc/dT observed in FeTe40/CdTe, indicating a substantial strain effect from CdTe. The variation in dc/dT can be attributed to the difference in thermal expansion between FeTe and the substrates. The smaller lateral thermal expansion of CdTe leads to an effective in-plane tensile strain in FeTe, which in turn enhances the out-of-plane thermal shrinkage in the films (Fig. S5). The Poisson ratios ν of FeTe1000/CdTe and FeTe40/CdTe, evaluated from the dc/dT slope, correspond to 0.4 and 0.5, respectively, showing an enhancement compared to the bulk value of 0.2³¹ (See Supplementary Information for more details). This enhanced Poisson ratio suggests a considerably strong coupling between FeTe and CdTe, which plays a crucial role in achieving the cramping effect that prevents the structural transition. Below T_s , the c -value of FeTe/CdTe films exhibits a clear split, with the tetragonal branch subsisting while a new branch appears in the monoclinic phase, as highlighted in the grey area of Fig. 3d. In this phase, c for all the films appears to approach the bulk value at low temperatures, suggesting complete lattice relaxation free from the strain.

To investigate the impact of substrate effects on the AFM order in FeTe, we performed first-principles calculations, where the in-plane lattice constant was fixed to mimic the substrate constraint (See Methods for more details). With decreasing $-\Delta c/c$, which corresponds to the uniaxial compressive strain along the c -axis, the Fe moments (μ) monotonously decreases, while the energy difference between the AFM and paramagnetic ground states, $E_{\text{AFM}} - E_{\text{PM}}$, increases (Fig. 3e). This is likely because the compressive strain along the c -axis enhances hopping via Te atoms, reducing electron correlations and making the AFM ordering less favourable. Indeed, in thinner FeTe/CdTe films, anomalies in magnetic susceptibility and the Hall coefficient at T_s , associated with the AFM ordering, become less pronounced¹⁷. These results suggest that the AFM ordering is considerably suppressed under the strong compressive strain along the c -axis.

It is informative to estimate the volume fraction of the monoclinic phase, $V_M/(V_T + V_M)$, where V_M and V_T represent the volumes of the monoclinic and tetragonal phases, respectively, derived from the integrated intensity of each Gaussian component in the θ - 2θ profiles. Figure 3f displays the T -dependence of $V_M/(V_T + V_M)$. For FeTe1000/STO, the monoclinic phase sharply develops below T_s and reaches nearly 100% within experimental detection limits below $T - 30$ K. In contrast, the monoclinic phase is significantly suppressed in FeTe/CdTe films, with $V_M/(V_T + V_M)$ reaching about 40% for FeTe1000/CdTe

and as low as 15% for FeTe40/CdTe. The $V_M/(V_T + V_M)$ value remains around 40% even for an FeTe200/CdTe film, suggesting that substantial suppression of the monoclinic phase requires films at least thinner than 200 nm (Fig. S6). These results suggest that the suppression of the monoclinic phase is due to the substrate cramping effect, which extends remarkably far into the FeTe film, influencing regions up to 600 nm from the interface in FeTe1000/CdTe, as illustrated in the inset of Fig. 3f. This is somewhat unexpected, as the higher-order epitaxy occurs only within a few UCs near the interface, yet it appears to stabilise the crystal structure over a remarkably large length. This strong coupling between the substrate and the film likely plays a crucial role in the substrate-selective superconductivity, as the strong out-of-plane compressive strain and the suppression of the monoclinic phase weaken the concomitant AFM order, which is known to compete with superconductivity²¹.

We next investigated the superconducting properties of FeTe/CdTe films and found that they exhibit distinct two-dimensional characteristics. Figure 4a shows the T -dependence of resistivity for $t = 10, 20, 40$ and 80 nm, where superconductivity is observed in all the films. This observation is consistent with our scenario that the superconductivity can emerge in films with suppressed tetragonal-to-monoclinic transition. Interestingly, the zero-resistivity critical temperature T_{c0} decreases with decreasing t , whereas the onset temperature T_c around 12 K is nearly independent of t . This nearly t -independent onset T_c suggests that the energy scale for superconducting gap formation is similar across all films. The broad superconducting transitions observed in thinner films are attributed to the Berezinskii-Kosterlitz-Thouless (BKT) transition, where strong fluctuations due to the low dimensionality prevent long-range order at finite temperatures. As shown in Fig. 4b and Fig. S7a, the temperature dependence of resistivity for the $t = 10, 20$ and 40 nm films is fitted by the Halperin-Nelson (HN) formula:

$$R = R_0 \exp \left[-2b \left(\frac{T_0 - T}{T - T_{\text{BKT}}} \right)^{1/2} \right], \quad (1)$$

where R_0 and b are material-dependent fitting parameters³². The fitting for the FeTe40/CdTe film yields $T_{\text{BKT}} = 5.8$ K. The current-voltage (I - V) characteristics for the FeTe40/CdTe film (Fig. 4c) show the power-law behaviour $V \propto I^\alpha$, as expected for two-dimensional superconductivity. The inset of Fig. 4c displays the T dependence of the exponent α , which crosses $\alpha = 3$ at around $T_{\text{BKT}} = 5.8$ K, as expected from the BKT theory.

Two-dimensional superconductivity in thin FeTe/CdTe films is further corroborated by the angle-dependence of the upper critical field H_{c2} . Figure 4d displays the polar angle θ dependence of H_{c2} , which is defined by the fields at which R reduces to half of the normal-state value. The H_{c2} of the FeTe40/CdTe film exhibits a distinct kink anomaly at $\theta = 90^\circ$, which is well captured by the two-dimensional Tinkham model, rather than the three-dimensional anisotropic mass model³³. In stark contrast, the θ -dependence of H_{c2} for the FeTe80/CdTe film agrees well with the three-dimensional model (Fig. S8c). At present, the origin of this crossover in superconducting dimensionality between $t = 40$ and 80 nm remains unclear. One possible explanation is that the interface hosts two-dimensional superconductivity, whereas the bulk of the FeTe film exhibits three-dimensional superconductivity whose T_{c0} exceeds that of the interface for thicknesses above 80 nm. The observation that thin FeTe/CdTe films exhibit two-dimensional superconductivity suggests the crucial role of the substrate effect in the emergence of superconductivity in this system.

The superconductivity observed in FeTe/CdTe is reminiscent of that reported in heterostructure systems where FeTe is interfaced with other tellurides³⁴, such as Bi₂Te₃-based compounds^{22,35–37}, MnBi₂Te₄³⁸, MnTe³⁹, and Fe₃GeTe₂⁴⁰. Superconductivity has also been observed in FeTe thin films grown via pulsed laser deposition, where tensile strain—similar to that observed in FeTe/CdTe—is argued to be crucial for inducing superconductivity⁴¹. However, in all these systems, including

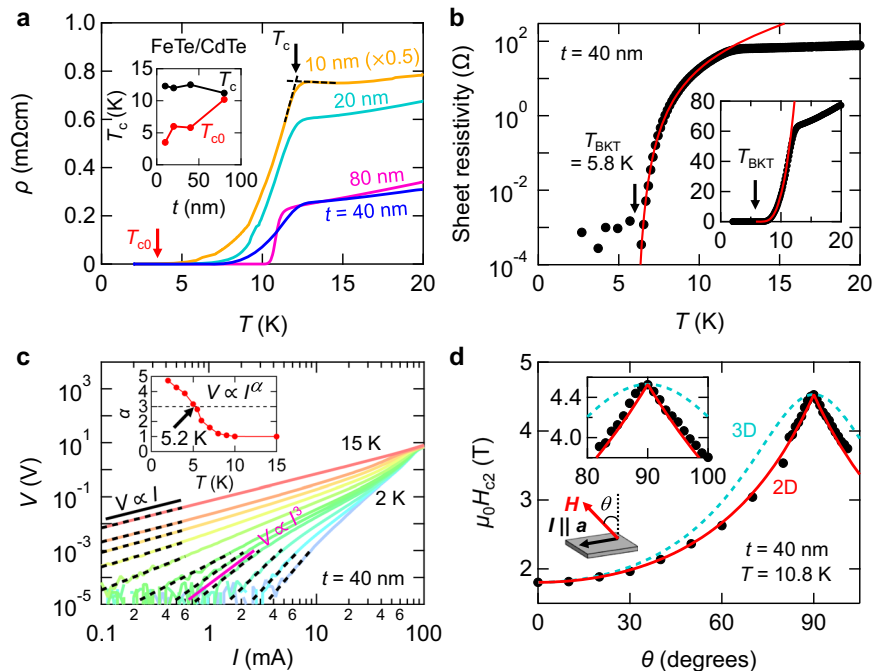


Fig. 4 | Two-dimensional superconductivity in FeTe/CdTe films. **a** Temperature dependence of resistivity with different thickness t . The black and red arrows indicate the onset and zero-resistivity critical temperatures, T_c and T_{c0} , respectively, for the $t = 10$ nm sample. The inset shows t dependence of T_c and T_{c0} . **b** Temperature dependence of sheet resistivity of the $t = 40$ nm thin film on logarithmic (main panel) and linear (inset) scales at zero field. The red curve represents fitting result using Halperin-Nelson (HN) formula with $T_{\text{BKT}} = 5.8$ K. **c** I - V curves in the log-log scale taken with 1-ms-pulsed currents. The measurements were

performed at $T = 2$ - 10 K in 1 K increments, and additionally at 5.5 K and 15 K. The dashed lines represent linear fittings. The solid black and magenta lines show slopes for $V \propto I$ and $V \propto I^{\alpha}$, respectively. The inset shows temperature dependence of α . The exponent crosses $\alpha = 3$ at around $T_{\text{BKT}} = 5.8$ K. **d** Polar angle θ dependence of H_{c2} . The red solid and cyan dashed lines represent the theoretical 2D Tinkham and 3D anisotropic mass models, respectively. The inset panel shows an expanded view around $\theta = 90^\circ$. The inset cartoon illustrates the experimental configuration.

heterostructures, structural investigation at low temperatures is lacking. To clarify the mechanism behind the emergence of superconductivity, future investigations are required to determine whether the tetragonal phase is preserved in these heterostructures or not.

Finally, we comment on potential applications of the higher-order epitaxial FeTe films. One major obstacle in investigating Majorana fermions in the topological superconductor candidate $\text{FeSe}_{0.45}\text{Te}_{0.55}$ solid solution is the inevitable inhomogeneity associated with Se/Te clustering. ARPES studies have revealed that topological surface states tend to appear in a Te-rich region⁴², highlighting the essential role of Te atoms in enhancing spin-orbit coupling. Inhomogeneity may also produce trivial conductance peaks at non-zero energies in scanning tunnelling spectroscopy experiments⁴³, which can mimic the zero-bias peaks expected from Majorana zero modes. Additionally, the superconducting properties of FeTe/CdTe appear similar to those of Te-rich FST films: it exhibits $T_c \sim 12$ K and relatively isotropic upper critical fields (Figs. S7c and S8b), similarly reported in Te-rich FST thin films grown on CdTe⁴⁴. A recent ARPES study revealed topological surface states in an $\text{FeSe}_{0.07}\text{Te}_{0.93}$ thin film⁴⁵, suggesting that topological states are preserved deep into the FeTe end of the series. These results suggest that the superconducting FeTe, with strong spin-orbit coupling yet free from compositional inhomogeneity, provides an ideal platform for investigating Majorana fermions.

Another intriguing direction of research involves the superlattice of interstitials in FeTe/CdTe, which breaks the translational symmetry of FeTe. Moiré patterns have been observed in one-UC FeTe films grown on Bi_2Te_3 ⁴⁶ and NbSe_2 ⁴⁷, where 8×2 -type and stripe-like patterns, distinct from the present 6×6 pattern on CdTe, are respectively resolved. Such superlattices may generate a long-range moiré-like potential, analogous to effects seen in twisted bilayer graphene⁴⁸, possibly modifying the electronic structure of the FeTe film near the

interface. As higher-order epitaxy can be applied to a wide range of materials systems, our MBE-based technique may provide a more robust and reproducible approach than exfoliation-based method to realising superstructures with periodic strain and potential, opening new ways to control the topological properties of materials and inducing quantum emergent phenomena^{12,13}.

Methods

Sample fabrication

All samples studied in this work were synthesised using the MBE method¹⁷. Prior to the synthesis, CdTe(001) substrates were etched with bromine-methanol (0.1% bromine) for 30 seconds, while STO substrates were annealed at 1000 °C for 10 hours under an O_2 flow. The films were synthesised at a substrate temperature of 240 °C in an ultrahigh vacuum chamber, with simultaneous beam fluxes of Fe and Te (plus Se for FST). The growth rate was approximately at 3 min/nm. After the growth, a Te-flux was continuously supplied for 30 minutes while samples cooled.

X-ray diffraction

We performed XRD for room-temperature characterisation of samples using SmartLab (RIGAKU) with $\text{Cu K}\alpha$ x-ray. All other low-temperature XRD data was taken with synchrotron x-ray source (12 keV) at Photon Factory beam line 4C, High Energy Accelerator Research Organization (KEK) in Japan.

Transport

We measured electrical transport properties with Quantum Design Physical Properties Measurement System (PPMS). We used indium soldering for electrical contact to films. The excitation current was fixed at 10 μA .

Scanning transmission electron microscopy

The samples were cut into lamellae using focused ion beam technique and cleaned with Ar ion beam. We performed STEM measurements with acceleration voltage of 200 kV using JEM-ARM200F (JEOL) at Foundation for Promotion of Material Science and Technology of Japan (MST).

First-principles calculations

We performed first-principles calculations to evaluate the impact of *c*-axis compression on the magnetic properties. The calculations were conducted using the projector augmented wave method implemented in the Vienna ab initio simulation package⁴⁹, with the generalised-gradient-approximation type exchange-correlation functional proposed by Perdew, Burke, and Ernzerhof⁵⁰. In our simulations, the lattice parameters were first fixed to the experimental values of the tetragonal phase of Fe_{1.11}Te: *a* = *b* = 3.8253 Å, *c* = 6.2787 Å, and *z*_{Te} = 0.28207¹⁹. We then systematically reduced the *c*-axis lattice parameter by *x*% (*x* = 0.5, 1.0, 1.5, 2.0, and 2.5) keeping all other structural parameters unchanged. All the calculations were performed within the magnetic UC (2 × 1 × 1 relative to the primitive cell), using a plane-wave cutoff energy of 500 eV, and a Monkhorst-Pack *k*-grid of 12 × 24 × 12.

Data availability

The source data used in this study have been deposited in Zenodo⁵¹.

References

- Arthur, J. R. Molecular beam epitaxy. *Surf. Sci.* **500**, 189–217 (2002).
- Goldman, A., Vas'ko, V., Kraus, P., Nikolaev, K. & Larkin, V. Cuprate/manganite heterostructures. *J. Magn. Magn. Mater.* **200**, 69–82 (1999).
- Pfeiffer, L. & West, K. The role of MBE in recent quantum Hall effect physics discoveries. *Physica E: Low Dimens. Syst. Nanostruct.* **20**, 57–64 (2003).
- Wang, Q.-Y. et al. Interface-induced high-temperature superconductivity in single unit-cell FeSe films on SrTiO₃. *Chin. Phys. Lett.* **29**, 037402 (2012).
- Tokura, Y., Yasuda, K. & Tsukazaki, A. Magnetic topological insulators. *Nat. Rev. Phys.* **1**, 126–143 (2019).
- Nunn, W., Truttman, T. K. & Jalan, B. A review of molecular-beam epitaxy of wide bandgap complex oxide semiconductors. *J. Mater. Res.* **36**, 4846–4864 (2021).
- Naritsuka, M., Terashima, T. & Matsuda, Y. Controlling unconventional superconductivity in artificially engineered *f*-electron Kondo superlattices. *J. Phys. Condens. Matter* **33**, 273001 (2021).
- Stoyanov, S. On the theory of epitaxial growth. *Surf. Sci.* **172**, 198–210 (1986).
- Narayan, J. & Larson, B. Domain epitaxy: A unified paradigm for thin film growth. *J. Appl. Phys.* **93**, 278–285 (2003).
- Springholz, G. & Wiesauer, K. Nanoscale dislocation patterning in PbTe/PbSe (001) lattice-mismatched heteroepitaxy. *Phys. Rev. Lett.* **88**, 015507 (2001).
- Estandía, S., Dix, N., Chisholm, M. F., Fina, I. & Sánchez, F. Domain-matching epitaxy of ferroelectric Hf_{0.5}Zr_{0.5}O₂ (111) on La_{2/3}Sr_{1/3}MnO₃ (001). *Cryst. Growth Des.* **20**, 3801–3806 (2020).
- Tang, E. & Fu, L. Strain-induced partially flat band, helical snake states and interface superconductivity in topological crystalline insulators. *Nat. Phys.* **10**, 964–969 (2014).
- Zeljko, I. et al. Strain engineering Dirac surface states in heteroepitaxial topological crystalline insulator thin films. *Nat. Nanotechnol.* **10**, 849–853 (2015).
- Wang, Z. et al. Topological nature of the FeSe_{0.5}Te_{0.5} superconductor. *Phys. Rev. B* **92**, 115119 (2015).
- Zhang, P. et al. Observation of topological superconductivity on the surface of an iron-based superconductor. *Science* **360**, 182–186 (2018).
- Wang, D. et al. Evidence for majorana bound states in an iron-based superconductor. *Science* **362**, 333–335 (2018).
- Sato, Y. et al. Molecular beam epitaxy of superconducting FeSe_xTe_{1-x} thin films interfaced with magnetic topological insulators. *Phys. Rev. Mater.* **8**, L041801 (2024).
- Nagahama, S. et al. Control of nonreciprocal charge transport in topological insulator/superconductor heterostructures by Fermi level tuning and superconducting layer thickness. *Phys. Rev. B* **112**, L121110 (2025).
- Koz, C., Röbber, S., Tsirlin, A. A., Wirth, S. & Schwarz, U. Low-temperature phase diagram of Fe_{1+y}Te studied using x-ray diffraction. *Phys. Rev. B* **88**, 094509 (2013).
- Bao, W. et al. Tunable ($\delta\pi$, $\delta\pi$)-type antiferromagnetic order in α -Fe(Te,Se) superconductors. *Phys. Rev. Lett.* **102**, 247001 (2009).
- Liu, T. et al. From (π , 0) magnetic order to superconductivity with (π , π) magnetic resonance in Fe_{1.02}Te_{1-x}Se_x. *Nat. Mater.* **9**, 718–720 (2010).
- Yasuda, K. et al. Nonreciprocal charge transport at topological insulator/superconductor interface. *Nat. Commun.* **10**, 2734 (2019).
- Telesca, D., Nie, Y., Budnick, J., Wells, B. & Sinkovic, B. Impact of valence states on the superconductivity of iron telluride and iron selenide films with incorporated oxygen. *Phys. Rev. B* **85**, 214517 (2012).
- Zhang, Z. et al. Superconductivity in Fe_{1.05}Te:O_x single crystals. *Phys. Rev. B* **88**, 214511 (2013).
- Li, F. et al. Atomically resolved FeSe/SrTiO₃(001) interface structure by scanning transmission electron microscopy. *2d Mater.* **3**, 024002 (2016).
- Peng, R. et al. Picoscale structural insight into superconductivity of monolayer FeSe/SrTiO₃. *Sci. Adv.* **6**, eaay4517 (2020).
- Obata, Y. et al. Chemical composition control at the substrate interface as the key for FeSe thin-film growth. *ACS Appl. Mater. Interfaces* **13**, 53162–53170 (2021).
- Terai, K. et al. In-plane lattice constant tuning of an oxide substrate with Ba_{1-x}Sr_xTiO₃ and BaTiO₃ buffer layers. *Appl. Phys. Lett.* **80**, 4437–4439 (2002).
- Ren, Z., Li, H., Zhao, H., Sharma, S. & Zeljkovic, I. Rotation of the dislocation grid in multilayer FeSe films and visualization of electronic nematic domains via orbital-selective tunneling. *Phys. Rev. Mater.* **6**, 124802 (2022).
- Xiao, Y. et al. Physical properties, crystal and magnetic structure of layered FeTe_{1-x}Se_x superconductors. *Eur. Phys. J. B* **82**, 113–121 (2011).
- Chandra, S. & Islam, A. Elastic properties of mono- and poly-crystalline PbO-type FeSe_{1-x}Te_x (*x* = 0–1.0): A first-principles study. *Physica C Supercond.* **470**, 2072–2075 (2010).
- Halperin, B. & Nelson, D. R. Resistive transition in superconducting films. *J. Low Temp. Phys.* **36**, 599–616 (1979).
- Tinkham, M. *Introduction to superconductivity* (Courier Corporation, 2004).
- Yao, X., Yi, H. T., Jain, D., Yuan, X. & Oh, S. Mystery of superconductivity in FeTe films and the role of neighboring layers. *APL Mater.* **13** (2025).
- He, Q. L. et al. Two-dimensional superconductivity at the interface of a Bi₂Te₃/FeTe heterostructure. *Nat. Commun.* **5**, 4247 (2014).
- Yao, X. et al. Hybrid symmetry epitaxy of the superconducting Fe(Te, Se) film on a topological insulator. *Nano Lett.* **21**, 6518–6524 (2021).
- Yi, H. et al. Interface-induced superconductivity in magnetic topological insulators. *Science* **383**, 634–639 (2024).
- Yuan, W. et al. Coexistence of superconductivity and antiferromagnetism in topological magnet MnBi₂Te₄ films. *Nano Lett.* **24**, 7962–7971 (2024).

39. Yao, X. et al. Superconducting fourfold Fe(Te, Se) film on sixfold magnetic MnTe via hybrid symmetry epitaxy. *Nano Lett.* **22**, 7522–7526 (2022).
40. Yi, H. T. et al. Universal superconductivity in FeTe and all-iron-based ferromagnetic superconductor heterostructures. *Adv. Funct. Mater.* 2418259 (2025).
41. Han, Y. et al. Superconductivity in iron telluride thin films under tensile stress. *Phys. Rev. Lett.* **104**, 017003 (2010).
42. Li, Y. et al. Electronic properties of the bulk and surface states of $\text{Fe}_{1+y}\text{Te}_{1-x}\text{Se}_x$. *Nat. Mater.* **20**, 1221–1227 (2021).
43. Machida, T. & Hanaguri, T. Searching for majorana quasiparticles at vortex cores in iron-based superconductors. *Prog. Theor. Exp. Phys.* ptad084 (2023).
44. Sato, Y. et al. Non-Fermi liquid transport and strong mass enhancement near the nematic quantum critical point in $\text{FeSe}_x\text{Te}_{1-x}$ thin films. *Phys. Rev. B* **112**, L041121 (2025).
45. Lin, H. et al. A topological superconductor tuned by electronic correlations. *arXiv preprint arXiv:2503.22888* (2025).
46. Qin, H. et al. Moiré superlattice-induced superconductivity in one-unit-cell FeTe. *Nano Lett.* **21**, 1327–1334 (2021).
47. Deng, H.-B. et al. Moiré superlattice modulations in single-unit-cell FeTe films grown on NbSe_2 single crystals. *Chinese Physics B* **30**, 126801 (2021).
48. Cao, Y. et al. Unconventional superconductivity in magic-angle graphene superlattices. *Nature* **556**, 43–50 (2018).
49. Kresse, G. & Furthmüller, J. Efficient iterative schemes for *ab initio* total-energy calculations using a plane-wave basis set. *Phys. Rev. B* **54**, 11169 (1996).
50. Perdew, J. P., Burke, K. & Ernzerhof, M. Generalized gradient approximation made simple. *Phys. Rev. Lett.* **77**, 3865 (1996).
51. Source data for “Superconductivity and suppressed monoclinic distortion in FeTe films enabled by higher-order epitaxy” <https://doi.org/10.5281/zenodo.17355459> (2025).
52. Momma, K. & Izumi, F. Vesta 3 for three-dimensional visualization of crystal, volumetric and morphology data. *J. Appl. Crystallogr.* **44**, 1272–1276 (2011).

Acknowledgements

We thank Xiuzhen Yu, Yingming Xie, Masataka Mogi, and Lixuan Tai for discussions. This work was supported by JSPS KAKENHI (Grant Numbers 24K17020 (Y.S.), 22K18965 (N.K.), 23H04017 (N.K.), 23H05431 (N.K. and Y.T.), 23H05462 (N.K.), 24H00417 (N.K.), 24H01652 (N.K.), and 25H02126 (N.K.)), JST FOREST (Grant Number JPMJFR2038 (N.K.)), JST CREST (Grant Numbers JPMJCR1874 (Y.T.) and JPMJCR2303 (N.K.)), Mitsubishi Foundation (N.K.), Sumitomo Foundation (N.K.), Tanaka Kikinzoku Memorial Foundation (N.K.), and the RIKEN TRIP initiative (Many-body Electron Systems). This work was performed under the approval of the Photon Factory Program Advisory Committee (Proposal No. 2022G551).

Author contributions

Y.T. conceived and supervised the project. Y.S. and S.N. synthesised samples with help from I.B., R.Y., M.Kawamura, A.T., N.K. and M.Kawasaki. Y.S. and S.N. performed transport and atomic force microscopy experiments. Y.S. conducted STEM experiments with MST. Y.S., S.N., S.K., and H.S. conducted x-ray diffraction experiments under the guidance of T.A. T.N. and R.A. performed the first-principles calculations. Y.S. analysed the data and all authors contributed to the interpretation. Y.S. wrote the manuscript with input from all authors.

Competing interests

The authors declare no competing interests.

Additional information

Supplementary information The online version contains supplementary material available at <https://doi.org/10.1038/s41467-025-65902-w>.

Correspondence and requests for materials should be addressed to Yuki Sato or Yoshinori Tokura.

Peer review information *Nature Communications* thanks Gan Wang and the other, anonymous, reviewer(s) for their contribution to the peer review of this work. A peer review file is available.

Reprints and permissions information is available at <http://www.nature.com/reprints>

Publisher's note Springer Nature remains neutral with regard to jurisdictional claims in published maps and institutional affiliations.

Open Access This article is licensed under a Creative Commons Attribution-NonCommercial-NoDerivatives 4.0 International License, which permits any non-commercial use, sharing, distribution and reproduction in any medium or format, as long as you give appropriate credit to the original author(s) and the source, provide a link to the Creative Commons licence, and indicate if you modified the licensed material. You do not have permission under this licence to share adapted material derived from this article or parts of it. The images or other third party material in this article are included in the article's Creative Commons licence, unless indicated otherwise in a credit line to the material. If material is not included in the article's Creative Commons licence and your intended use is not permitted by statutory regulation or exceeds the permitted use, you will need to obtain permission directly from the copyright holder. To view a copy of this licence, visit <http://creativecommons.org/licenses/by-nc-nd/4.0/>.

© The Author(s) 2025